Solute Drag Creep in Niobium Alloy C103 (Nb-10Hf-1Ti) at 1550 to 1750 °C

THOMAS J. BENNETT IV and ERIC M. TALEFF

Data are presented from tensile tests of commercial Nb-based alloy C103 (Nb-10Hf-1Ti, by wt pct) at temperatures of 1550–1750 °C and true-strain rates of 3×10^{-5} to 3×10^{-3} s^{-1}. Changes in strain rate generated pronounced short-term transients in flow stress. These transients are of the inverse type characteristic of solute drag creep (SDC). C103 produced large tensile elongations of 150–200 pct and strain hardened during plastic deformation. Test data provide an average strain-rate sensitivity of 0.29 and an activation energy for creep of 340 kJ/mol. Short-term transient data indicate a stress dependence for dislocation glide velocity of $\bar{v} \propto \sigma^{2.7}$ and for mobile dislocation density of $\rho \propto \sigma^{0.7}$. The deformed microstructure contains indistinct subgrains and steep strain gradients. All data indicate deformation by SDC controlled by the diffusion of Hf solute atoms for the range of conditions examined. Data from plastic flow transients suggest that creep rates for C103 available in the literature are likely from the primary creep region. When that is considered, data from the literature and the present study are in good agreement.

https://doi.org/10.1007/s11661-024-07617-z

I. INTRODUCTION

THIS study investigates the mechanisms responsible for plastic flow in commercial Nb-based alloy C103 (Nb-10Hf-1Ti, by wt pct)[1] at temperatures from 1550 to 1750 °C. C103 was identified by Wadsworth and co-workers[2,3] as belonging to a special group of alloys called Class I solid-solution alloys,[4–6] also called Class A alloys.[7,8] Class I alloys demonstrate significant solid-solution strengthening at high homologous temperatures, a desirable behavior not available in Class II alloys even at very high solute concentrations.[4,6] The mechanism responsible for Class I alloy behavior involves solute atoms producing a drag force on gliding edge dislocations.[9–13] This mechanism is termed solute drag creep (SDC). It requires solute atoms that have a significant size misfit with the lattice and a relatively high solubility, which limits SDC to a rather small number of alloys.[4–8] SDC does not require any secondary phases, and it produces an inverted creep primary that significantly reduces initial creep rate compared to the normal primary creep behavior characteristic of Class II alloys. SDC creep also produces a high strain-rate sensitivity, typically approaching a value of one-third, that is insensitive to grain size and can lead to large tensile elongations, sometimes in excess of 100 pct. Improving understanding of SDC and its effects in C103 will provide benefits beyond the processing and application of this alloy alone. Because C103 is representative of other Class I refractory metal alloys,[3] improved understanding for C103 will benefit the development and utilization of this larger group of refractory metal alloys.

The present study provides new data for C103 from tensile tests at temperatures of 1550–1750 °C and strain rates from 3×10^{-5} to 3×10^{-3} s^{-1}. New data are also presented from the characterization of microstructures produced by deformation during testing. The primary goal of this study is to better understand SDC and its effects in C103 across these test conditions. This requires data for short-term transient plastic flow responses and for the microstructures produced during deformation. Such data were not available prior to the present study and are essential to interpreting data in the literature from creep tests of C103. Secondary goals of this study include measuring parameters important to high-temperature deformation, such as strain-rate sensitivity and the activation energy for creep. Because evaluating short-term transient plastic flow behaviors is essential to the present study, and these behaviors may not be familiar to all readers, they are briefly reviewed here.

Class I and Class II alloys produce distinctly different transient plastic flow behaviors. These can be understood through the classical creep curve, which is divided

THOMAS J. BENNETT IV and ERIC M. TALEFF are with the Department of Mechanical Engineering, University of Texas at Austin, 204 East Dean Keeton St., Stop C2200, Austin, TX 78712. Contact e-mail: thomas.bennett@utexas.edu
Manuscript submitted July 12, 2024; accepted September 25, 2024.
Article published online October 21, 2024

into three stages: primary, secondary, and tertiary creep.[4] Primary creep is the short-term transient response upon initial loading of a specimen. The top row of Figure 1 demonstrates primary creep behaviors for (a) Class I and (b) Class II alloys immediately after loading in a classical creep test, which controls load to apply either a constant engineering stress or a constant true stress. Because pure metals exhibit the same type of primary creep behavior as Class II alloys, the curve shown in (b) is called a *standard* primary. It is characterized by an initially fast creep rate that slows into secondary creep. The *inverted* primary behavior of Class I alloys shown in (a) produces an initially slow creep rate that accelerates into secondary creep. This slow initial creep rate is very desirable for creep resistance. Instead of controlling load, tests in the present study controlled displacement rate to achieve constant true-strain rates. This type of test produces the short-term transient responses shown in the bottom row of Figure 1 for (c) Class I and (d) Class II alloys. The magnitude of each plastic flow transient and its rate of decay are easier to measure in this test than in a classical creep test. Because plastic flow transients from classical creep tests must be characterized using strain rate, which is the time derivative of the directly measured displacement, it can be difficult to distinguish the transition from primary to secondary creep. Reporting of creep rates from Class I alloys is especially problematic because the minimum creep rate occurs at the beginning of loading, not during secondary creep. For this reason, it is not always possible to know the degree to which a reported creep rate is affected by transient behavior. Data from rate-controlled tests are less ambiguous because transients are characterized using flow stress calculated from load, which is directly measured. By imposing a series of true-strain rates, short-term plastic flow transient responses can be measured across several rates in a single specimen. Such strain-rate-change tests are employed in the present study.

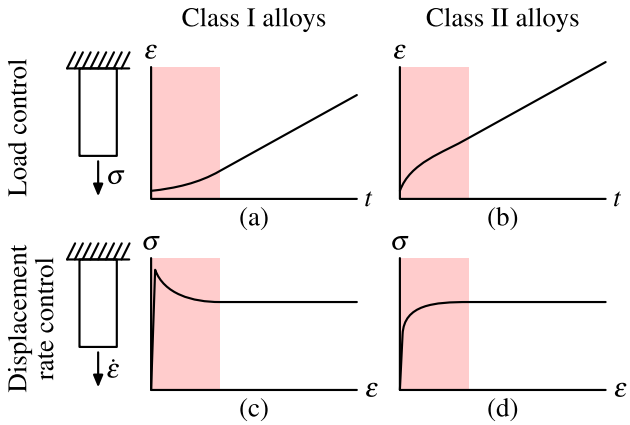

Fig. 1—Short-term transient responses in plastic flow at the beginning of tensile tests for Class I and Class II alloys are illustrated for both load-controlled and displacement-rate-controlled tests. The transient region is highlighted in each plot.

Intelligent interpretation of deformation mechanisms requires some knowledge of microstructure. Because in-situ observations of microstructure at the temperatures of interest to this study are not a practical possibility, care was taken to preserve microstructure that is representative of that during deformation at elevated temperature. Microstructure is characterized using the recently developed technique of combined backscattered electron (CBSE) imaging.[14] The CBSE technique provides useful visualizations of subgrains and plastic strain gradients, the features of greatest relevance to the deformation mechanism identified for C103 in the present study.

II. EXPERIMENTAL PROCEDURES

A sheet of wrought niobium alloy C103 (Nb-10Hf-1Ti) meeting the ASTM B654-10 standard[15] was acquired with a thickness of 1.5 mm in the cold-worked, as-rolled condition. The chemical composition of the material reported by the vendor is provided in Table I. Tensile tests were conducted on this material under vacuum at temperatures from 1550 to 1750 °C using the following procedures. Tensile specimens were excised from the sheet material in a dog-bone geometry with the tensile axis along the sheet rolling direction (RD) using water-jet cutting. Tensile specimens were produced with a gauge length of 25.4 mm, a gauge width of 6.4 mm, a grip-gauge transition radius of 1.6 mm, and the original sheet thickness of 1.5 mm. A single hole of 6.4 mm in diameter was centered in each grip end to accommodate SiC pins for loading during tensile testing. Tensile tests were conducted in a vacuum furnace using an electro-mechanical load frame with computer control and data acquisition. Each specimen was held under a load of 22 N while being heated to the desired test temperature in the vacuum furnace to keep the load train taught during thermal expansion. Once at the desired test temperature, which took from 15 to 40 minutes, the specimen was held at this temperature for one hour to allow temperature equilibration throughout the load train prior to tensile straining; this prevents thermal expansion from adversely affecting the calculation of strain. Because the recrystallization temperature of C103 is approximately 1200 °C,[1] full recrystallization of the C103 specimen is expected during this step. During tensile testing, temperature was controlled to within

Table I. Composition of the C103 Material in wt pct

Nb	Hf	Ti	Zr	Ta	W	O	C	N	H
Bal	10.28	1.18	0.45	0.42	0.3	0.02	0.0049	0.0049	< 0.001

± 10 °C, as determined through independent temperature calibration tests, and a vacuum level of approximately 10^{-5} torr was maintained. Two types of tensile tests were conducted across temperatures of 1550, 1650, and 1750 °C. Two tensile tests were conducted to rupture at 1650 °C and a constant true-strain rate, one test at $10^{-3}\,s^{-1}$ and the other at $10^{-4}\,s^{-1}$. Cross-head velocity was controlled to achieve a constant true-strain rate assuming constant specimen volume and uniform elongation, after accounting for the effect of thermal expansion on the specimen initial gauge length. Four strain-rate-change (SRC) tensile tests were conducted, two at 1650 °C and one each at 1550 and 1750 °C. For each SRC test, a series of discrete true-strain rates was applied to a specimen held at a constant temperature. For this study, ten steps in true-strain rate were applied sequentially for a true strain of 0.05 per step. True-strain rates were varied in the range of 3×10^{-5} to $3 \times 10^{-3}\,s^{-1}$. At the end of each tensile test, furnace power was quickly turned off to provide the most rapid specimen cooling possible. The furnace cooled to below 1000 °C within two to three minutes. For SRC tests, a constant load approximately equal to that of the final SRC step was maintained during cooling to preserve the deformed microstructure. Load and cross-head displacement were measured throughout each test. Load readings from a load cell external to the vacuum furnace were corrected to remove the force from bellows connecting the load train to the vacuum furnace. Data acquired from independent tests of bellows force under vacuum as a function of cross-head displacement were used to make this correction. Tensile data were corrected for compliance of the load train by enforcing the known elastic modulus of Nb at the temperature of testing.[16–18] Stress and strain were calculated throughout each test from these data. Additional details of the instrumentation used for these experiments are described by Brady[19] and Noell.[20]

Metallography was conducted to observe microstructures of the C103 material in the as-received condition, after annealing without deformation at 1650 °C, and after tensile deformation at 1650 °C. Metallographic specimens were excised from the grip and central gauge regions of a specimen subjected to a SRC test at 1650 °C. The grip region provided material that was annealed without deformation, and the gauge region provided material deformed in tension to a true strain of approximately 0.5 and held under load during cooling to preserve, as much as reasonably possible, the microstructure produced during deformation at the elevated temperature. Metallographic specimens were also excised from the middle of the gauge region in the specimen tested to rupture at 1650 °C and $10^{-4}\,s^{-1}$. Because this ruptured specimen could not be held under load during cooling, its microstructure was statically annealed immediately following rupture and during the initial stages of cooling. Pieces from the as-received and the tested materials were arranged with three different orientations in metallographic mounts for observation. Specimens were viewed along the RD, long-transverse direction (LTD), and short-transverse direction (STD). Metallographic specimens were prepared by sequential grinding on progressively finer SiC papers and then polished using sequentially finer diamond suspensions. Final polishing was conducted using a 0.05 μm colloidal silica solution on a vibratory polisher. Polished specimens were observed in a Tescan Vega3 scanning electron microscope (SEM) using secondary electron imaging and backscattered electron (BSE) imaging. Energy-dispersive spectroscopy (EDS) was used to measure the elemental compositions of specific microstructural features. For selected specimens, three

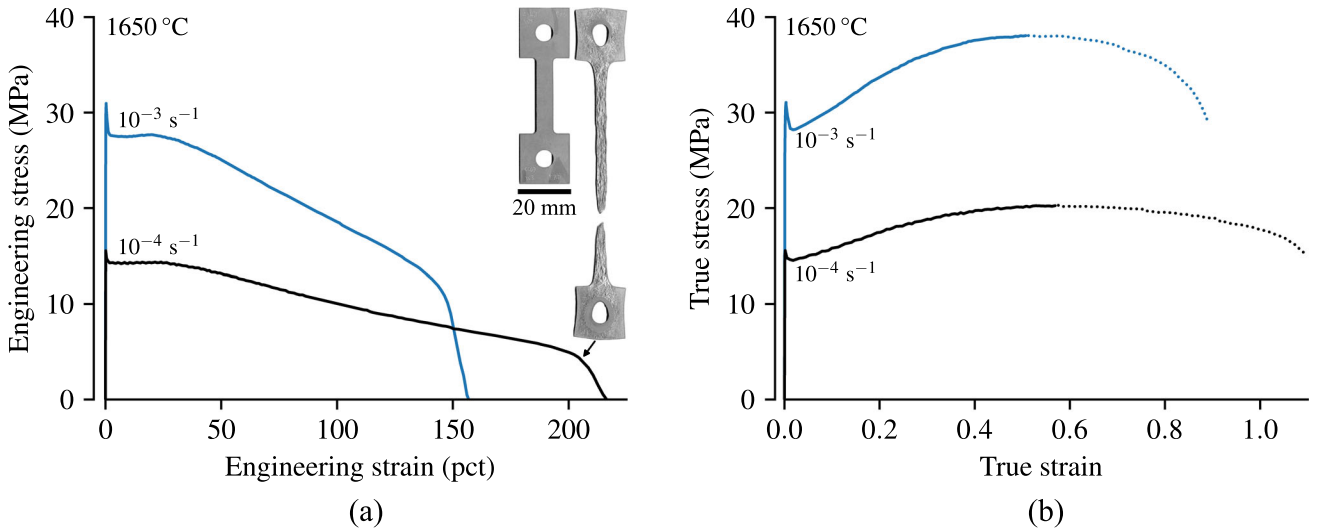

Fig. 2—Tensile data acquired at 1650 °C are presented (*a*) as engineering stress against engineering strain and (*b*) as true stress against true strain for tests at true-strain rates of 10^{-3} and $10^{-4}\,s^{-1}$. A tensile coupon is shown in (a) before and after tensile testing at 1650 °C and $10^{-4}\,s^{-1}$.

BSE images were acquired from the same field of view at slightly different tilts of −1, 0, and +1°. These three images were used to produce a combined BSE (CBSE) data set for viewing as a colorized image using the method described by Bennett and Taleff.[14] A single BSE image may not reveal all grain boundaries because adjacent grains do not always present a distinct difference in channeling contrast for a single BSE imaging geometry. The CBSE technique largely overcomes this limitation by combining data from multiple imaging geometries. CBSE data have the additional benefit of providing better distinction of substructure and strain gradients than possible with a single BSE image.

III. RESULTS

A. *Mechanical Test Data*

Data from the two tensile tests to rupture at 1650 °C are presented in Figure 2. Data are shown as engineering stress against engineering strain in Figure 2(a) for true-strain rates of 10^{-3} and $10^{-4}\,s^{-1}$. These tests produced elongations exceeding 150 and 200 pct, respectively. Inset in Figure 2(a) are images of an untested specimen and the specimen tested to rupture at $10^{-4}\,s^{-1}$. Rupture occurred by gradual necking to a sharp edge without any macroscopic indications of cavity nucleation and growth. The rough surface of the tested specimen suggests a coarse grain size that led to inhomogeneous deformation. This is referred to as the orange peel effect[21] and can occur at both low and high temperatures. Stress transients of short duration occurred upon initial straining in both tests. Decay of these transient stresses occurred within just a couple percent strain. The slow neck development in these tests allows true stress and true strain to be reasonably calculated to quite large strains. True stress is plotted against true strain in Figure 2(b). Calculations of these values assume constant volume and uniform elongation. Data following the maximum calculated true stresses, which occur at true strains near 0.5, are plotted as dotted curves to indicate where the assumption of uniform elongation may no longer be reasonable. Note that the flow localization associated with necking does not commence at a particular strain in strain-rate-hardening materials. Instead, necking proceeds gradually throughout tensile deformation, with the rate of neck growth decreasing as strain-rate sensitivity increases.[22,23] Although necking is likely controlled primarily by the strain-rate sensitivity under these test conditions, some strain hardening follows the initial stress transients. The tensile data of Figure 2 indicate that true stress and true strain can be reasonably calculated up to a large strain of approximately 0.5, which supports the validity of conducting SRC tests up to this same strain.

Data from one of the SRC tests conducted at 1650 °C are presented in Figure 3 as true stress plotted against true strain. The entire SRC test is shown in Figure 3(a) with each step and its true-strain rate noted. All SRC tests used an identical series of steps in true-strain rate. Figure 3(b) presents only the data from the fourth SRC step in (a) to demonstrate the values measured and calculated for each step. For each SRC step, the peak flow stress of the initial transient, σ_p, and the fully relaxed flow stress at the end of that step, σ_{end}, were measured. Measurements of σ_{end} were made by averaging the flow stress within the final 0.01 range of true strains at the end of each SRC step. The peak flow stress, σ_p, was measured as the maximum or minimum flow stress that followed each rate change, depending on whether strain rate was increased or decreased. The relaxed stress at the start of the transient, σ_{start}, and the initial transient stress size, $\Delta\sigma_0$, were calculated using a procedure that will be described with data reduction methods. Necking was not observed in any SRC test specimens after testing, but all exhibited some extent of

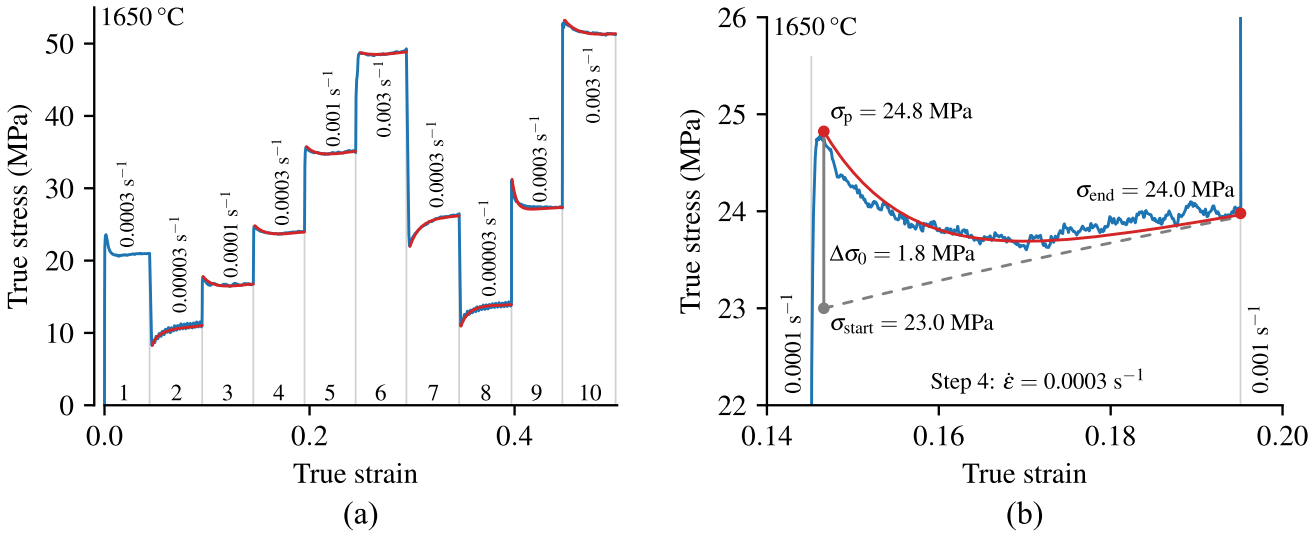

Fig. 3—(*a*) Data from a strain-rate-change (SRC) test at 1650 °C are presented as true stress against true strain. The rate of each step is indicated. Curves fit to the transients after rate changes are shown in red. (*b*) Data from step 4 of this SRC test are plotted with quantities measured and calculated for this step labeled (Color figure online).

surface roughness from the orange peel effect. The severity of surface roughness increased with increasing test temperature. Data extracted from all four SRC tests are provided in Appendix A.

B. *Microstructure*

The as-received material presented a uniform cold-worked microstructure without any significant second-phase particles, as demonstrated in the BSE image of Figure 4(a). After testing at elevated temperature, despite the maintenance of a vacuum, second-phase particles were evident to a depth of approximately 100 μm from the specimen surfaces. These are demonstrated in Figure 4(b), which presents a cross section through the gauge region of a specimen after a SRC test at 1650 °C to a true strain of 0.5. Both images in Figure 4 present the RD as horizontal and the STD, spanning the full sheet thickness of both specimens, as vertical. The tensile axis is along the RD, horizontal, in (b). Spot EDS analysis of particles near the specimen surface indicated a composition of primarily Hf and O in an atomic ratio of approximately 1:2, with a trace of Zr and no observable Ti. These results suggest that the second-phase particles are primarily HfO_2. Because the particle-containing layers comprise only 15 pct of the specimen thickness, these are not expected to significantly affect the mechanical properties measured from tensile tests.

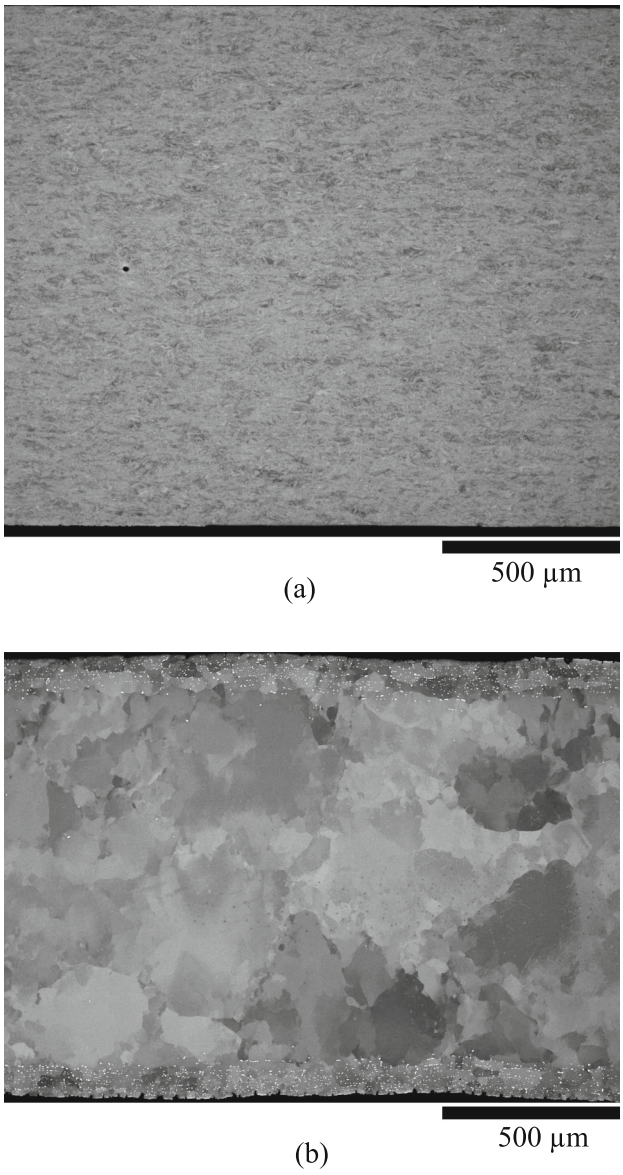

Fig. 4—BSE images show (*a*) the as-received material and (*b*) the deformed gauge region of a specimen after a SRC test at 1650 °C to a true strain of 0.5. The short-transverse direction (STD) is vertical, and the rolling direction (RD) is horizontal for both images. The tensile axis is the same as the RD in (b). The full thickness of the sheet is encompassed in the vertical direction of both images.

Figure 5 presents microstructures in specimens tested at 1650 °C imaged as colorized CBSE data. All images are oriented with the RD, the same as the tensile axis, vertical, and the LTD horizontal. Figure 5(a) is the microstructure in the undeformed grip region of a specimen after a SRC test at 1650 °C. Sharp changes in color indicate grain boundaries. Gradual changes in color across grains primarily occur because of electron channeling effects from small changes in the angle of incidence of the electron beam as it scans across the specimen.[14] This microstructure demonstrates complete recrystallization and a rather large grain size. An average lineal intercept grain size of $\ell = 370$ μm was measured using the rectangular planimetric (Saltykov) method to determine average grain area, which was then converted to equivalent lineal intercept grain size, all using the methods described in ASTM E112-13.[24,25] Figure 5(b) is the microstructure in the deformed gauge region of the same specimen shown in (a). In this image, sharp changes in color indicate grain boundaries or subgrain boundaries, which are low-angle boundaries typically formed during creep deformation.[4] Color gradients across short lengths generally indicate local plastic strain gradients induced during deformation. These are preserved because the SRC test specimen was held under load during cooling, thus reducing the relaxation of these microstructural features. The deformed microstructure in Figure 5(b) contains subgrains that are less uniform in size and shape and have less distinct boundaries than subgrains produced by hot deformation of unalloyed Nb.[26] Steep strain gradients are also evident. These features are consistent with a microstructure produced by SDC after significant strain. Figure 5(c) presents the microstructure in the specimen tested to rupture at 1650 °C and $10^{-4}\ s^{-1}$. Because this specimen was unloaded by rupture, it experienced static annealing from rupture until it cooled significantly below the test temperature. Although the microstructure before rupture was likely similar to that shown in (b), static annealing produced the coarser microstructure shown in (c), which contains fewer, larger subgrains with more distinct boundaries and no steep strain gradients. The presence of subgrains suggests that the microstructure in (c) was produced by static recovery, as opposed to static recrystallization.

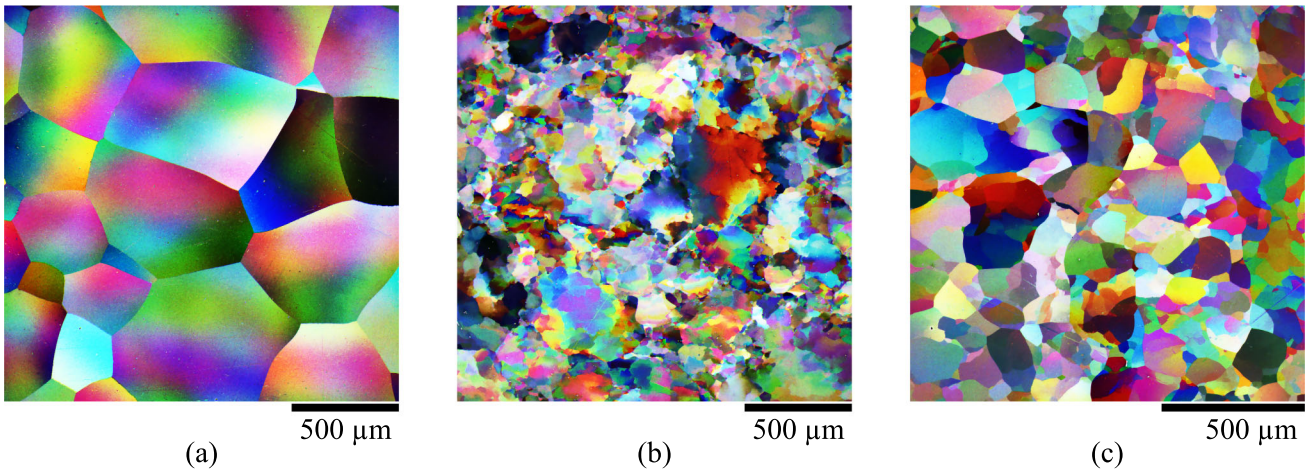

Fig. 5—Colorized CBSE images show (*a*) the undeformed grip region and (*b*) the deformed gauge region of a specimen after a SRC test at 1650 °C to a true strain of 0.5. A colorized CBSE image shows (*c*) the deformed gauge region of the specimen tested to rupture at 1650 °C and $10^{-4}\,s^{-1}$. In all images the rolling direction (RD), which coincides with the tensile axis, is vertical, and the long-transverse direction (LTD) is horizontal.

C. *Data Reduction*

To determine parameters important for understanding plastic flow in C103, a modified version of the phenomenological equation for creep[4] was applied to the reduction of experimental data. A modification to account for strain hardening was made to better interpret SRC data, which extend to large strains. Another modification was made to account for stress transients following rate changes in SRC data. Mechanical test data were interpreted through the following model for the true flow stress, σ, normalized by the temperature-dependent dynamic unrelaxed elastic Young's modulus, E,

$$\frac{\sigma}{E} = A\,\epsilon^{N}\,\dot{\epsilon}^{m}\,\exp\left(\frac{mQ_c}{RT}\right) + \frac{\Delta\sigma}{E}\ , \qquad [1]$$

where ϵ is true strain, $\dot{\epsilon}$ is true-strain rate, and T is absolute temperature. This model incorporates strain hardening through the Hollomon strain hardening exponent N, strain-rate sensitivity m, an activation energy for creep Q_c, and the material-dependent parameter A. R is the universal gas constant. The short-term transient stress $\Delta\sigma$ accounts for the stress transients following strain rate changes during testing. In the *relaxed* condition following the decay of short-term transient effects, $\Delta\sigma \approx 0$. Experimental data were first used to calculate the following parameters for the relaxed condition: N, m, Q_c, and A, in that order. Transient behaviors will be addressed after presenting the determination of these parameters.

The strain hardening exponent, N, was calculated first using data from the two tensile tests to rupture. Each test provides data at a constant temperature and a constant true-strain rate. Considering only the relaxed condition, Eq. [1] provides the following relationship for calculating N at constant temperature and true-strain rate,

$$N = \left.\frac{\partial \ln(\sigma/E)}{\partial \ln(\epsilon)}\right|_{\dot{\epsilon},T}\ . \qquad [2]$$

Experimental data from the tensile tests to rupture at 1650 °C are plotted in Figure 6 as solid curves on axes of $\ln(\sigma/E)$ against $\ln\epsilon$. Normalization of stress should use temperature-dependent values of the dynamic, unrelaxed elastic modulus,[27,28] but only quasistatic data for the elastic modulus of C103 are available.[29,30] Thus, values of E for untextured, polycrystalline Nb were calculated from the fit to dynamic data of Armstrong and coauthors[16,17] recommended by Brady and Taleff[18] for temperatures above 1300 K,

$$E = 104.9 - 8.3513\times10^{-9}\,(T-1300)^{3.154}\ , \qquad [3]$$

where E is in GPa and T is in K. To ensure data are from the relaxed condition, only true strains from 0.04 up to the maximum calculated true stress were considered. The slope of the data on these axes equals N, the strain hardening exponent. The average value of the strain hardening exponent is $N = 0.141 \pm 0.003$, with uncertainty represented by the maximum difference between the average and the values individually fit using each tensile test to rupture. Round markers in Figure 6 show the relaxed stress, σ_{end}, at its corresponding true strain for each strain-rate step from all SRC tests. The straight lines presented in Figure 6 are linear fits to data at each temperature and true-strain rate assuming a fixed slope of $N = 0.141$. This value of N determined from the tests to rupture accurately describes the data from SRC tests across their wide range of temperatures and strain rates. Because of this, N was assumed constant across these conditions.

The strain-rate sensitivity, m, was calculated next. Equation [1] taken at constant true strain and

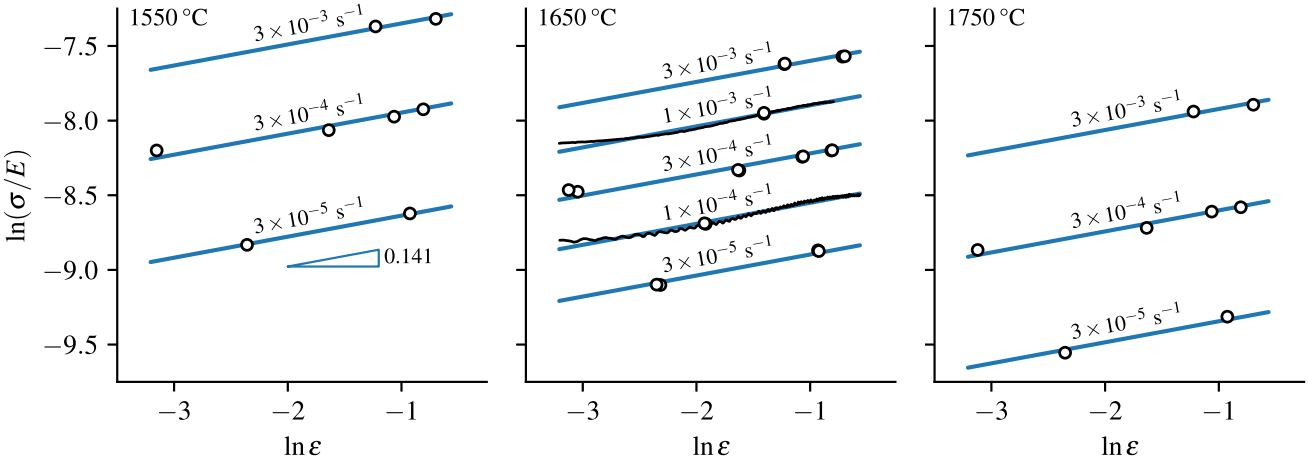

Fig. 6—Data are plotted as $\ln(\sigma/E)$ against $\ln\epsilon$ for constant true-strain rates at temperatures of 1550 °C, 1650 °C, and 1750 °C. Data from tensile tests to rupture are plotted as solid curves, and data from SRC tests are plotted as open symbols. Straight lines present fits, all of identical slope $N = 0.141$, to data at each temperature and strain rate.

temperature for the relaxed condition provides the following relation for the strain-rate sensitivity,

$$m = \left.\frac{\partial \ln(\sigma/E)}{\partial \ln \dot{\epsilon}}\right|_{\epsilon,T}. \quad [4]$$

The fits presented in Figure 6 were used to calculate values of $\ln(\sigma/E)$ at a constant true strain. Because these fits have identical slopes, the difference in $\ln(\sigma/E)$ values calculated between data at different rates for a constant temperature is invariant with the choice of strain. For convenience, $\ln(\sigma/E)$ was calculated at each temperature and true-strain rate for $\ln\epsilon = 0$ ($\epsilon = 1$). If a constant slope was not imposed for these fits, then it would be necessary to choose strain values in the range of actual data, a note of caution to bear in mind. Figure 7 presents the resulting values for $\ln(\sigma/E)$ against $\ln\dot{\epsilon}$. The slope of these data equals the strain-rate sensitivity, m. The average slope from data at all three temperatures is $m = 0.29 \pm 0.03$, with uncertainty represented by the maximum difference between the average and the most extreme individual slope measurement, including variation by the standard error calculated on that measurement. The linear fits shown in Figure 7 assume $m = 0.29$ at all temperatures. Note that the stress exponent, which is the inverse of the strain-rate sensitivity, is $n = 3.4$.

The activation energy for creep, Q_c, was calculated next. Equation [1] taken at constant true strain and true-strain rate in the relaxed condition provides the following relation for calculating the activation energy,

$$Q_c = \frac{R}{m}\left.\frac{\partial \ln(\sigma/E)}{\partial (1/T)}\right|_{\epsilon,\dot{\epsilon}}. \quad [5]$$

The linear fits shown in Figure 7 provide a convenient means of calculating values of $\ln(\sigma/E)$ at constant strain and strain rate. Because those fits enforce identical slopes, the differences between $\ln(\sigma/E)$ values at different temperatures are insensitive to the choice of strain rate. For convenience, values of $\ln(\sigma/E)$ were calculated

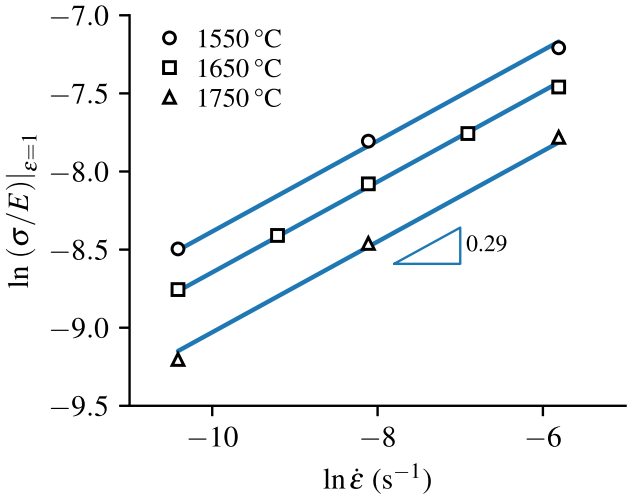

Fig. 7—Data are plotted as $\ln(\sigma/E)$ extrapolated to $\epsilon = 1$ against $\ln\dot{\epsilon}$ for each test temperature. Straight lines are fits, all of identical slope $m = 0.29$, to the data.

at $\ln\dot{\epsilon} = 0$ ($\dot{\epsilon} = 1\,\text{s}^{-1}$) and $\epsilon = 1$. A similar note of caution to that given for the calculation of m applies here. If a constant slope was not imposed on the linear fits in Figure 7, then rates within those spanned by the data must be used to calculate values of $\ln(\sigma/E)$. The calculated values of $\ln(\sigma/E)$ at $\dot{\epsilon} = 1\,\text{s}^{-1}$ and $\epsilon = 1$ are plotted against $1/T$ in Figure 8. The slope of these data is proportional to the activation energy, which was calculated to be $Q_c = (340 \pm 47)$ kJ/mol, with the uncertainty estimated as the standard error on the slope of the linear fit in Figure 8.

The fitted values of N, m, and Q_c were used with data from the SRC tests to calculate the A parameter. Data for the relaxed condition in every SRC step of all four SRC tests were used with Eq. [1] to calculate an average value of $A = (6.52 \pm 0.11) \times 10^{-6}\,\text{s}^{0.29}$, where uncertainty is represented by the 95 pct confidence interval.

The stress transient in each step of SRC test data following the first, *i.e.*, steps 2 through 10 of Figure 3(a), was evaluated after determining the parameters in Eq. [1] for the relaxed condition. This required first calculating σ_{start} and $\Delta\sigma_0$ for each step, as demonstrated in Figure 3(b), and then fitting a curve to the decaying transient stress. The relaxed stress, σ_{start}, at the same strain as the transient peak was extrapolated from the relaxed stress measured at the end of the SRC step, σ_{end}, by accounting for strain hardening during the SRC step. This calculation proceeded as follows:

$$\sigma_{\text{start}} = \sigma_{\text{end}} \left(\frac{\epsilon start}{\epsilon_{\text{end}}} \right)^N , \qquad [6]$$

where ϵ_{start} is the strain at the transient peak, and ϵ_{end} is the strain at the end of the SRC step. The initial size of the stress transient was then calculated as $\Delta\sigma_0 = \sigma_{\text{p}} - \sigma_{\text{start}}$. This value is positive when strain rate is increased and negative for a decreased strain rate.

The stress transient following each rate change was then modeled as an exponential decay, while accounting for strain hardening, as described by,

$$\Delta\sigma = \sigma - \sigma_{\text{start}} \left(\frac{\epsilon}{\epsilon_{\text{start}}} \right)^N \approx \Delta\sigma_0 \exp\left(- \frac{\epsilon - \epsilon start}{\eta} \right) . \qquad [7]$$

Here, η is a decay constant. The decay constant η can be interpreted as the strain following the transient peak at which the transient stress has decayed to $1/e \approx 37$ pct of its peak value. Because all other parameters were previously calculated, fitting Equation [7] to experimental data required fitting only the η parameter to the transient of each SRC step.

Inspecting data reduction results demonstrated that the sizes of the initial stress transients at the fastest SRC step rate of $10^{-3}\,\text{s}^{-1}$, steps 6 and 10 in Figure 3(a), were relatively small compared to the other SRC steps. The decay constants were also larger for these steps than for steps to the slower rates. For this reason, the onset of power-law-breakdown (PLB) was considered.[4] PLB generally occurs when $\dot{\epsilon}/D \geq 10^{13}\,\text{m}^2/\text{s}$, where D is the coefficient of lattice diffusion. Because no data are available for the diffusion of Hf in Nb, which might be the most appropriate diffusivity for creep deformation of C103, the lattice self-diffusion coefficient for Nb[31–33] was used to estimate the strain rates at which PLB might be expected. It was estimated that PLB begins at strain rates from 7×10^{-4} to $7 \times 10^{-3}\,\text{s}^{-1}$ for the test temperatures considered. PLB may explain the smaller stress transients observed at the fastest strain rate of the SRC tests. For this reason, only data from step changes to rates slower than $3 \times 10^{-3}\,\text{s}^{-1}$ were further considered for the analysis of transient behaviors. Excluding data from steps 6 and 10, the average value of the decay constant from all SRC test data was calculated as $\eta = (8.1 \pm 1.1) \times 10^{-3}$, where uncertainty is represented by the 95 pct confidence interval. The average value of η for steps to faster strain rates, 8.9×10^{-3}, was marginally greater than for steps to slower strain rate, 7.3×10^{-3}, but this difference is probably not statistically significant. The decay constant appears to decrease slightly with increasing temperature, as shown in Figure 9, which presents η plotted against temperature. Error bars indicate 95 pct confidence intervals. The Pearson correlation coefficient between η and T is -0.45, suggesting a weak negative correlation. The results from fitting parameters in Equations [1] and [7] to the experimental data are summarized in Table II.

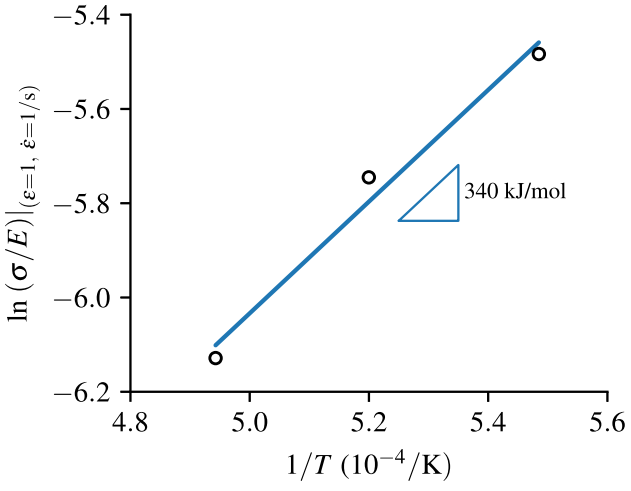

Fig. 8—Data are plotted as $\ln(\sigma/E)$ at a constant true strain ($\epsilon = 1$) and a constant true-strain rate ($\dot{\epsilon} = 1\,\text{s}^{-1}$) against $1/T$. The slope is proportional to the activation energy for creep.

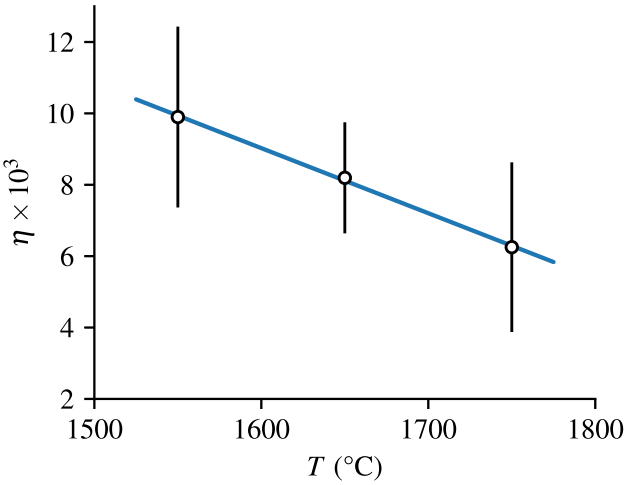

Fig. 9—The decay constant η is plotted as a function of test temperature. Error bars indicate the 95 pct confidence interval on each average value of η.

Table II. Creep Model Parameters for C103

$N = 0.141 \pm 0.003$
$m = 0.29 \pm 0.03$
$Q_c = (340 \pm 47)$ kJ/mol
$A = (6.52 \pm 0.11) \times 10^{-6}\,\text{s}^{0.29}$
$\eta = (8.1 \pm 1.1) \times 10^{-3}$

IV. DISCUSSION

The data produced at temperatures from 1550 to 1750 °C provide three key observations new to the mechanical metallurgy of Nb alloy C103. First is the observation of strain hardening during plastic flow at these temperatures, demonstrated in Figures 2(b) and 6. Strain hardening during SDC has received little previous attention and is not predicted by prior work that often assumed steady-state flow with negligible strain hardening.[4–8,34–42] The mechanistic source of strain hardening in C103 at these temperatures is not known, but possible sources include texture hardening.[43] The presence of strain hardening is an intriguing indication of much yet to learn about the plastic flow of solid-solution alloys at high temperatures. Knowing that strain hardening is present requires accounting for its effect when measuring other material parameters, such as m and Q_c. The second new observation is of microstructure produced in C103 during deformation. The deformed microstructure presents the indistinct subgrain structure and short-range deformation gradients expected from SDC after significant strain, approximately 0.5 true strain in the case of Figure 5(b). This is important evidence in support of SDC as the governing deformation mechanism under the conditions studied. The third new observation is of short-term stress transients following strain-rate changes, as demonstrated in Figure 3. The characterization of these transients from strain-rate-controlled tests provides strong evidence that deformation is governed by SDC, and it demands a reevaluation of creep data for C103 in the literature produced using stress-controlled tests. In the following discussion, these new observations are used to improve understanding for the plastic deformation of C103 in the context of data from the present study and data available in the literature.

A. *Evidence for Solute Drag Creep*

Data from the present study support arguments made in previous studies for SDC as the most likely mechanism governing deformation in C103 at elevated temperatures.[2,3,44] Titran and Klopp[44] made this identification based on measuring a stress exponent of 2.87 ($m = 0.35$) in their creep data acquired at temperatures ranging from 827 to 1204 °C. These temperatures are significantly lower than those of the present study and those investigated by Wadsworth *et al.*,[2] who also identified SDC in C103. Wadsworth *et al.* obtained creep data at temperatures from 1593 to 1694 °C and identified SDC as the governing creep mechanism based on: 1. large tensile elongations, often exceeding the capacity of their instrumentation, 2. a stress exponent of 3.4 ($m = 0.29$), identical to that determined in the present study, 3. inverted primary creep, 4. and an activation energy for creep of 316 kJ/mol, which is lower than that for lattice self-diffusion. They interpreted their activation energy for creep as likely equivalent to the activation energy for the diffusion of Hf solute atoms in the Nb lattice. Unfortunately, no data are available for Hf diffusion in Nb against which their interpretation for Q_c might be tested. The present study reinforces all the previously cited evidence for SDC in C103. Large tensile elongations of 150–200 pct were produced and were not limited by instrumentation. An average strain-rate sensitivity of 0.29 was confirmed across a broader range of temperatures and strain rates than were available to Wadsworth *et al.* The activation energy for creep measured in C103 (340 kJ/mol) agrees, to within measurement uncertainty, with those from Titran and Klopp (374 or 336 kJ/mol, depending on calculation method) and Wadsworth *et al.* (316 kJ/mol). All are lower than the activation energies reported for lattice self-diffusion in Nb across the temperatures of the present study, which were reported as 402 kJ/mol by Lundy *et al.*[31] and as ranging from 400 kJ/mol at 1550 °C to 412 kJ/mol at 1750 °C by Einziger *et al.*[32] All the measured activation energies for creep in C103 are less than the activation energy for creep in unalloyed Nb of 454 kJ/mol measured by Brady and Taleff .[18]

A deformed microstructure produced by SDC in C103 is presented in Figure 5(b). Deformation by SDC is supported by comparing this microstructure against that expected if deformation were by five-power dislocation creep, which produces a microstructure of small distinct subgrains.[4,5] Flow stress is inversely proportional to subgrain size under five-power creep, and this relation is generally insensitive to grain size, strain, and temperature.[4,5,45–50] Data from Brady and Taleff for the creep of unalloyed Nb,[18,26] both ASTM Type 1 and Type 2,[51] can be used to predict the subgrain size required for five-power creep to produce the flow stress of 51 MPa in C103 at the end of step 10 of a SRC test conducted at 1650°C. This is the test condition that produced the microstructure shown in Figure 5(b). Creep data from unalloyed Nb present a (lineal intercept) subgrain size of 27 μm for a flow stress of 19 MPa in Nb Type 1 and a subgrain size of 18 μm for a flow stress of 35 MPa in Nb Type 2. Based on these measurements, a subgrain size of 10 to 12 μm is necessary to sustain a flow stress of 51 MPa under five-power creep. Even the finest of the subgrains observed in Figure 5(b), approximately 25 μm and larger, are more than twice that size. This is evidence against the presence of five-power creep as a significant contributor to plastic flow and support for interpreting the deformed microstructure as consistent with deformation by SDC.

As previously argued by Wadsworth *et al.*,[3] solute drag behavior in C103 is primarily caused by its Hf content, not by Ti or Zr. Values of activation energy alone are insufficient for this determination. The activation energies for Ti and Zr solute diffusion in Nb are reported as 364–370 kJ/mol for Ti and 364 kJ/mol for Zr.[33,52] Although no data are available for Hf solute diffusion in Nb, the simulations of Zou *et al.*[53] predict an activation energy for Hf diffusion in Nb that is within 2 pct of those for Ti and Zr diffusion in Nb. All these activation energies agree well with the activation energy of 340 kJ/mol measured for plastic flow in C103. However, a significant solute drag effect requires a large size misfit of the solute atom in the solvent lattice and a

concentration of solute atoms sufficient to produce drag on moving dislocations.[6,7,9,10,54] The atomic volume size factor for Ti in Nb, $\Omega_{sf}^{\mathrm{Nb-Ti}} = -3.0$ pct,[55] is too small in magnitude to produce SDC. The atomic volume size factors for Zr and Hf in Nb, $\Omega_{sf}^{\mathrm{Nb-Zr}} = +27.11$ pct and $\Omega_{sf}^{\mathrm{Nb-Hf}} = +18.58$ pct[55] are both sufficiently large to produce SDC, with Zr presenting the greater likely effect per solute atom. It is the small atomic concentration of Zr in C103, 0.48 at pct, that makes it unlikely Zr could be responsible for the solute drag behaviors observed. The actual concentration of Zr in solid solution is likely even lower because of the propensity for Zr to scavenge interstitial elements.[30,56] The absence of a significant solute drag effect from 1 wt pct Zr is confirmed by inspecting data in the literature for binary Nb alloys containing this amount of Zr.[3,29,57–59] Data for Nb-1Zr (wt pct) alloys in the literature demonstrate neither the high strain-rate sensitivity nor the large tensile elongations expected from SDC.[3] SDC might, however, be induced by Zr at much higher concentrations, as is suggested by the marked increase in tensile elongation with rising temperature demonstrated by Schmidt and Ogden in an alloy of Nb containing 5 wt pct Zr.[29]

B. *The Solute Drag Creep Mechanism*

Data from stress transients in the present study confirm prior evidence for inverted primary creep and enable a deeper investigation of SDC in C103 than previously possible. SRC data may be interpreted through the Orowan equation[60] for conditions of constant temperature when dislocation density is invariant with plastic strain. For each such condition,

$$\dot{\epsilon} = B\,\rho(\sigma)\,\bar{v}(\sigma)\ , \qquad [8]$$

where mobile dislocation density, ρ, and average dislocation glide velocity, $\bar{v}$, are both functions of the applied stress and B is a constant of proportionality. Each SRC step provides two conditions in which dislocation density may be reasonably assumed invariant with strain. The first is at the peak of the stress transient immediately following a rate change, where the dislocation density may be assumed the same as immediately before the rate change. This provides a so-called *constant structure* test,[4,12,13,40,61] which can be used to probe the dependence of dislocation glide velocity on stress. The second is the relaxed condition after the stress transient is fully decayed, for which dislocation density is expected to be constant under a steady-state flow stress, interpreted here as equivalent to the relaxed stress. Data from this condition may be compared between different strain rates to probe the dependence of dislocation density on the relaxed stress. The dependencies on stress in Equation [8] can be tested against experimental data by measuring the *instantaneous* strain-rate sensitivity, m^*, and the *relaxed* strain-rate sensitivity, m, using a method previously introduced for this purpose.[40,61] The instantaneous strain-rate sensitivity is determined by comparing the stress of the peak after a rate change to the relaxed flow stress before that rate change. Define the true-strain rates before and after a rate change as $\dot{\epsilon}_1$ and $\dot{\epsilon}_2$, respectively. Then define the relaxed stress before the rate change as $\sigma_{1(\mathrm{end})}$. Taking $\sigma_{2(\mathrm{p})}$ as the peak stress after the rate change provides the instantaneous strain-rate sensitivity as,[40,61]

$$m^* = \left(\frac{d\ln\bar{v}}{d\ln\sigma}\right)^{-1} = \left.\frac{\partial\ln\sigma}{\partial\ln\dot{\epsilon}}\right|_{\rho} \approx \frac{\log_{10}\left(\sigma_{2\,(\mathrm{p})}/\sigma_{1\,(\mathrm{end})}\right)}{\log_{10}(\dot{\epsilon}_2/\dot{\epsilon}_1)}\ . \qquad [9]$$

Taking $\sigma_{2(\mathrm{start})}$ as the relaxed flow stress immediately after the rate change, previously calculated as σ_{start} after each rate change using Equation [6], provides the relaxed strain-rate sensitivity as,

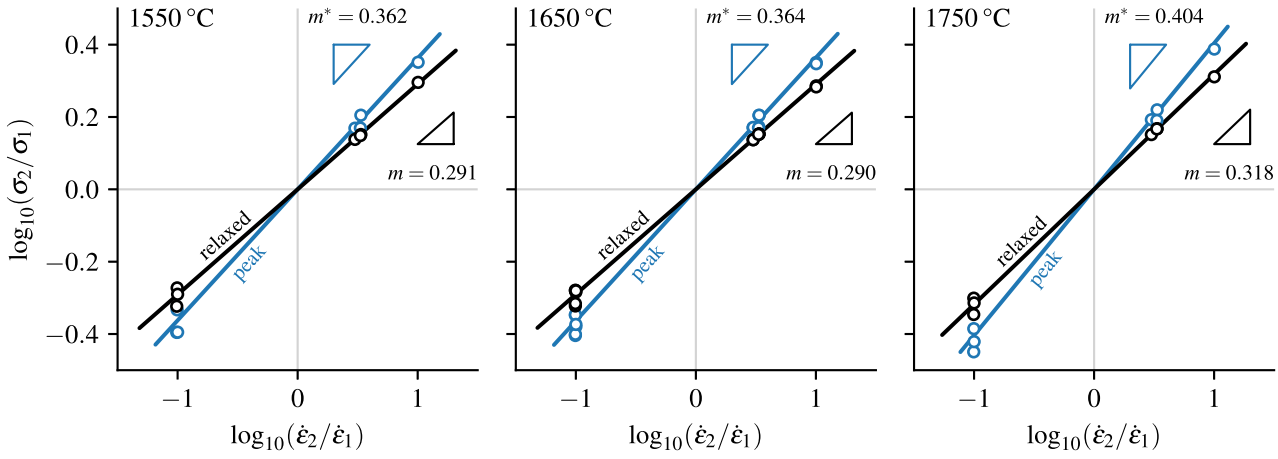

Fig. 10—Stress transient data are presented as the logarithm of the stress change ratio against the logarithm of the imposed strain-rate ratio. The instantaneous strain-rate sensitivity, m^*, and the relaxed strain-rate sensitivity, m, are calculated from the slopes of the data.

$$m = \left(\frac{d\ln\rho}{d\ln\sigma} + \frac{1}{m^*}\right)^{-1} = \left.\frac{\partial\ln\sigma}{\partial\ln\dot{\epsilon}}\right|_{\text{relaxed}} \approx \frac{\log_{10}\left(\sigma_{2\,(\text{start})}/\sigma_{1\,(\text{end})}\right)}{\log_{10}(\dot{\epsilon}_2/\dot{\epsilon}_1)} \ . \quad [10]$$

Figure 10 presents stress transient data as the logarithm of the ratio of stresses after and before rate changes against the logarithm of the ratio of strain rates after and before rate changes. The slope of data for peak stresses is equal to m^*, and the slope of data for relaxed stresses is equal to m. Data predicted to be in the PLB regime are excluded from Figure 10. Taking the measurements for m^* and m in Figure 10 and weighting their averages by the number of SRC step measurements made at each temperature provides $m^* = 0.374$ and $m = 0.297$, the latter being within the measurement uncertainty of the value measured in Figure 7. It is noted from Figure 10 that m increases slightly to 0.318 at the highest test temperature of 1750°C. These data produce the following dependencies for dislocation glide velocity and dislocation density on flow stress,[40]

$$\bar{v} = B_{\bar{v}}\,\sigma^{\frac{1}{m^*}} = B_{\bar{v}}\,\sigma^{2.7} \quad [11]$$

$$\rho = B_\rho\,\sigma^{\left(\frac{1}{m}-\frac{1}{m^*}\right)} = B_\rho\,\sigma^{0.7} \ , \quad [12]$$

where $B_{\bar{v}}$ and B_ρ are constants of proportionality for a given temperature. Applying Equations [11] and [12] to Equation [8] demonstrates that the stress exponent is $n = 2.7 + 0.7 = 3.4$, as previously measured. It is of note that data for SDC in Al-Mg alloys produced similar values for m and m^*.[12,13,40] These dependencies demonstrated from experimental data should be held in mind during future investigations into the mechanisms that control SDC in refractory alloys.

Models developed for SDC require assuming substructures containing specific dislocation configurations that evolve during deformation.[9–13] Weertman[9,10] developed the most widely used model for SDC that correctly predicts the stress exponent of 3 and activation energies corresponding with solute diffusion generally observed for SDC by considering the drag force from solute atoms on gliding dislocations and the density of dislocation sources. Weertman[10] invoked the model for solute drag on gliding dislocations developed by Cottrell and Jaswon,[54] which predicts a dislocation glide velocity directly proportional to the applied stress and the solute diffusivity, $\bar{v} \propto D_{\text{sol}}\,\sigma$. Weertman assumed a dependence of dislocation density on stress from a particular configuration of dislocation loop sources,[9] but an identical result is also produced by assuming the Taylor relation[62] to predict a dislocation density that varies with the square of the applied stress, $\rho \propto \sigma^2$. Together with Equation [8], these reproduce the aspects of Weertman's model relevant to the present study,

$$\dot{\epsilon} = B_{\text{SDC}}\,D_{\text{sol}}\,\sigma^3 \ , \quad [13]$$

where B_{SDC} incorporates all other important information, including the influence of the temperature-dependent elastic modulus and solute atom size misfit in the lattice. Although experimental data for SDC generally follow Equation [13], they contradict this theory by indicating a stronger dependence of the dislocation glide velocity on applied stress and a weaker dependence for the dislocation density. A subsequent model by Mills *et al.*[12,13] which extended the model of Takeuchi and Argon,[11] considered a dislocation loop along which the edge component experiences solute drag during glide and the screw component does not. This model predicts values of $m = \frac{1}{3}$ and $m^* = \frac{1}{2}$, which better agree with mechanical test data. However, it is not clear which dislocation configurations assumed among these models, if any, agree with physical reality. It is difficult to envision further progress in understanding the mechanisms responsible for SDC without new data for the substructures it actually produces. In seeking such data, the importance of experimentally preserving microstructure evolved during high-temperature deformation must be carefully addressed, a point made by comparing the microstructures in Figures 5(b) and (c).

C. *Comparisons with Literature Data*

It is instructive to compare data from the present study produced using strain-rate-controlled tests to data available from prior studies documented in the literature, most of which used creep tests that controlled stress. The challenge with such a comparison is that the creep rates reported in the literature are typically either initial creep rates or minimum creep rates. The decay constant measured in the present study, see Table II, demonstrates that transient creep behavior likely persists for at least 1–2 pct strain following initial loading or a change in loading conditions. Creep rates reported in the literature were likely measured within this range of strains, where transient behavior can be significant. The measured creep rates are thus slower than those that would follow the relaxation of transient behavior, as indicated in Figure 1(a). Unfortunately, it is not possible to calculate the degree of relaxation when the creep rate was measured or to predict the creep rate that would have been measured in the relaxed condition. This makes it impossible to compare data at identical degrees of relaxation or in a uniformly unrelaxed condition. For these reasons, literature data are compared in Figure 11 as reported by their authors with data of the present study in the relaxed condition for stresses calculated at engineering strains of both 2 and 50 pct. It is important to bear in mind that the transient stress would increase the flow stresses plotted for the present study by 10 pct or more. Data are presented in Figure 11 as a plot of the logarithm of the Zener–Hollomon parameter,[63]

$$Z = \dot{\epsilon} \times \exp\left(\frac{Q_c}{RT}\right) \ , \quad [14]$$

calculated using an activation energy of 340 kJ/mol, against the logarithm of flow stress compensated by the temperature-dependent, dynamic, unrelaxed elastic Young's modulus, calculated as recommended by Brady and Taleff.[18] The slope of data in this plot is equal to the stress exponent, n. These data demonstrate a stress

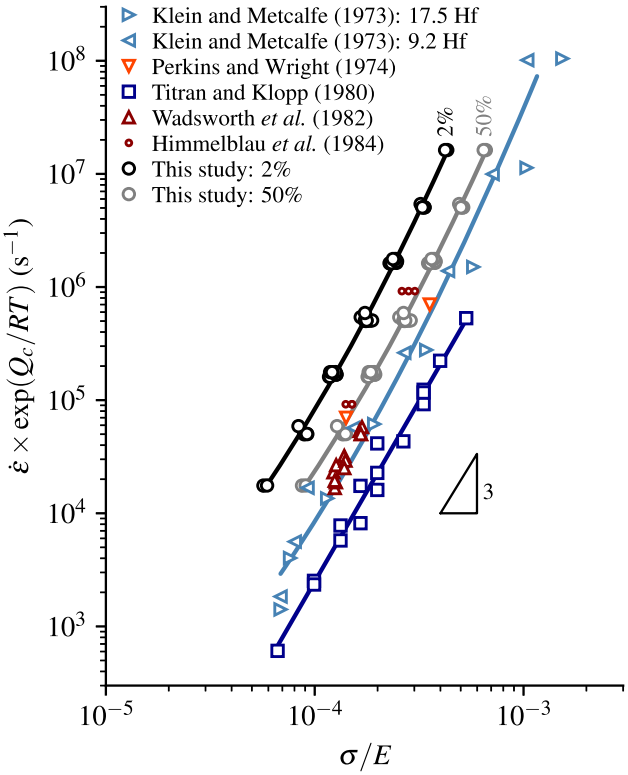

Fig. 11—Data are plotted as the Zener–Hollomon parameter, Z, against σ/E on dual logarithmic scales. Data from the present investigation are presented as relaxed stresses at engineering strains of 2 and 50 pct. Data from the literature are plotted using the creep rates reported by their authors[2,44,64–66].

exponent of approximately three that gradually increases as temperature decreases and strain rate increases, *i.e.*, as Z increases.

Four sets of creep data for C103 and similar alloys tested under vacuum are available in the literature for comparison against data from the present study. Klein and Metcalfe[64] produced creep data for a range of Nb-based binary alloys at temperatures from 870 to 1900 °C. These included alloys containing 9.2 and 17.6 wt pct Hf, which are similar enough to the Hf content of C103 to merit comparison. Klein and Metcalfe used an unusual creep testing technique, which they called their "single specimen" technique. They heated a single specimen first to the lowest of their desired test temperatures and then increased load until a creep rate of 10^{-5} s^{-1} was obtained. The temperature of the specimen was then raised to a new, higher temperature, and the process was repeated until the range of desired temperatures was spanned with data from the single specimen. Although they used a Fullman *et al.* type of loading arm[67] to produce accurate measurements of applied true stress despite specimen elongation during testing, their measurements of creep rate were likely within the range of strains before complete relaxation of transient behavior. Perkins and Wright[65] reported creep test data for uncoated C103 at 1480 and 1650 °C for strains up to 2 pct. Titran and Klopp[44] reported the largest set of creep data for C103 but only covered temperatures from 827 to 1204 °C. Their creep tests were conducted to maximum strains that ranged from only 0.96–4.11pct. They reported the "initial tertiary creep rate," which is the creep rate immediately after loading, and the time to 1 pct strain. The creep rate from the latter is faster than the former by an average of 2.1 times, with the difference in individual tests ranging from 1.2 to 5.6 times. Wadsworth *et al.* reported minimum creep rates for C103 tested at temperatures of 1593, 1650, and 1693 °C. Figure 11 presents creep data from all four literature sources acquired at temperatures of 1000 °C and higher. Data are plotted directly as reported by Klein and Metcalfe and as reported by Wadsworth *et al.* The data from Perkins and Wright measured at 2 pct strain are plotted. The data from Titran and Klopp measured at 1 pct strain are plotted. Himmelblau *et al.*[66] conducted rate-controlled tensile tests of C103 at 1650 °C and reported yield strength for two different cross-head displacement rates. Their data are included in Figure 11 as reported. Kumawat *et al.*[68] reported tensile yield and ultimate strengths for C103 at temperatures up to 1500 °C from rate-controlled tests with an initial strain rate of 10^{-1} s^{-1}. Because these conditions place their data well into PLB and produce Zener–Hollomon parameters of $Z > 10^9$ s^{-1}, their data are not plotted in Figure 11. For all data, the Zener–Hollomon parameter was calculated using the 340 kJ/mol activation energy for creep measured in the present study.

The data presented in Figure 11 provide evidence for several important characteristics of plastic deformation in C103 at elevated temperatures. An activation energy of 340 kJ/mol collapses experimental data neatly onto a single curve for each study. The data from Klein and Metcalfe and from Titran and Klopp demonstrate the applicability of this activation energy at temperatures down to 1000 °C. All experimental data present a stress exponent of approximately three that gradually increases with increasing Z. Data for the binary Nb-Hf alloys of Klein and Metcalfe and data for C103 from Perkins and Wright and from Wadsworth *et al.* rest approximately together on a common curve. This might be expected because the creep rates reported in these three studies were all measured in a similar manner. These observations strongly support the conclusion of Wadsworth *et al.*[2,3] that creep in these materials is controlled by SDC and the activation energy for creep is equivalent to that for the diffusion of Hf solute atoms in Nb. The data from Titran and Klopp diverge from the other literature data in the direction of slower strain rates, lower Z. This may be more a result of the small strains of their experiments producing strain rates slowed by transient behavior than from the lower temperatures of their tests, particularly because the data from Klein and Metcalfe cover the same range of temperatures. The data for binary Nb-Hf alloys from Klein and Metcalfe are especially interesting. Their Nb-9.2Hf and Nb-17.5Hf alloys present nearly identical creep behaviors at low Z and diverge only slightly at high Z, with the alloy containing less Hf becoming slightly weaker than the alloy with more Hf. This suggests that dislocations are saturated with Hf during

SDC in both alloys. Similar observations were made for other Class I alloys, in which additional solute concentration beyond that necessary to saturate dislocations during SDC produced no additional strengthening.[6–8] Klein and Metcalfe also presented data from a Nb-4.7Hf alloy, not plotted here, that was significantly weaker than Nb-9.2Hf under similar test conditions. This indicates that the concentration of Hf necessary to saturate dislocations in Nb during SDC is between 4.7 and 9.2 wt pct. Considering the propensity of Hf to be consumed in forming HfO_2, as shown near the specimen surface in Figure 4(b), those interested in manufacturing C103 components should take particular care to evaluate the concentration of Hf retained in solid solution. Too little Hf in solution risks the loss of creep strengthening from SDC. This is important to the additive manufacturing approaches of recent interest for C103 component production[69–74] because controlling oxygen levels in these processes can be difficult. Data plotted from the present study using relaxed stresses lie to the left of creep data from the literature in Figure 11, as expected. Data for relaxed stresses calculated at 50 pct strain approach creep data from the literature and would likely overlap them if transient effects were included. However, the data for C103 from Himmelblau *et al.*,[66] which were also obtained using rate-controlled testing, are within the range of values provided by the present investigation. These complications demonstrate why reporting minimum creep rate, yield stress, or other simple measures of plastic flow behavior alone is inadequate to developing a deep understanding of plasticity in Class I alloys at elevated temperatures. But within this limitation, data from the literature and the present study are remarkably consistent.

V. CONCLUSIONS

Tensile tests were performed on wrought C103 (Nb-10Hf-1Ti) sheet under strain-rate control at temperatures from 1550 to 1750 °C. The resulting data for mechanical behaviors, characterization of relevant microstructures, and comparisons to data from the literature led to the following conclusions.

1. The parameters measured to describe high-temperature plastic deformation and the microstructures observed following deformation are consistent with plasticity controlled by solute drag creep (SDC) in C103. The rate controlling step in SDC is likely Hf solute atom diffusion. Comparisons with literature data indicate that SDC controls deformation in both C103 and binary Nb-Hf alloys with similar or higher Hf concentrations across conditions characterized by Zener–Hollomon parameters in the range of $10^3 \leq Z \leq 10^8\,s^{-1}$.
2. Wrought C103 exhibits strain hardening with a strain-hardening exponent of 0.141 across the temperatures and strain rates examined.
3. The average strain-rate sensitivity of C103 is 0.29 across the conditions examined. Strain-rate sensitivity increases slightly at the highest test temperature of 1750 °C.
4. The activation energy for creep across the conditions examined is 340 kJ/mol. Data from the literature indicate that this value is likely valid at temperatures down to 1000 °C. This activation energy is expected to approximately equal that for Hf solute atom diffusion in Nb.
5. Pronounced, short-term stress transients of the inverse type occur after strain-rate changes. The decay constant measured for these stress transients suggests that 1–2 pct strain is necessary for a transient to relax. The duration of short-term transient responses has important ramifications for correctly interpreting data from classical creep tests. Measurements of both initial and minimum creep rates from such load-controlled tests are likely to include the short-term transient response and indicate creep rates substantially slower than during secondary or steady-state creep. Differentiation between transient and relaxed behaviors in data from the rate-controlled tests of the present study is accomplished without such ambiguity.
6. The average dislocation glide velocity depends on flow stress as $\bar{v} \propto \sigma^{2.7}$, and mobile dislocation density depends on flow stress as $\rho \propto \sigma^{0.7}$ during SDC in C103.
7. Accounting for the effects expected from short-term creep transients and differences in testing methodologies, data from the present study and data from the literature are in good agreement.

ACKNOWLEDGMENTS

The authors gratefully acknowledge support from the National Science Foundation under grant DMR-2003312 and instrumentation under grant DMR-9974476. The authors gratefully acknowledge useful guidance from Dr. S. L. Semiatin of MRL Materials Resources LLC, Xenia Township, OH. The authors thank Ms. Andrea Kalani for assistance with metallography for this study.

CONFLICT OF INTEREST

The authors declare that they have no conflict of interest.

APPENDIX A

See Table III.

Table III. Data from SRC Tests

T (°C)	Step	$\dot{\epsilon}$ (s^{-1})	ϵ_{end}	σ_{end} (MPa)	σ_p (MPa)	σ_{start} (MPa)	$\Delta\sigma_0$ (MPa)	η (10^{-3})
1550	1	3.05×10^{-4}	0.04	28.0	32.8			
	2	3.00×10^{-5}	0.09	14.9	11.2	13.3	− 2.0	7.2
	3	1.01×10^{-4}	0.14	22.4	23.8	21.1	2.8	11.4
	4	3.03×10^{-4}	0.19	32.0	33.0	30.7	2.3	12.9
	5	1.01×10^{-3}	0.24	46.6	47.3	45.1	2.2	12.2
	6	3.03×10^{-3}	0.29	64.2	63.5	62.5	1.0	17.5
	7	3.00×10^{-4}	0.34	35.1	29.8	34.3	− 4.5	11.0
	8	3.00×10^{-5}	0.40	18.3	14.1	18.0	− 3.9	9.1
	9	3.03×10^{-4}	0.45	36.8	41.2	36.2	5.0	5.5
	10	3.03×10^{-3}	0.50	67.5	69.4	66.4	2.9	15.8
1650	1	3.01×10^{-4}	0.05	20.7	22.9			
	2	2.99×10^{-5}	0.10	11.1	8.2	10.0	− 1.8	4.9
	3	1.00×10^{-4}	0.15	16.7	17.8	15.8	2.0	10.6
	4	3.02×10^{-4}	0.20	23.9	24.8	22.9	1.9	11.4
	5	1.00×10^{-3}	0.25	34.9	35.3	33.9	1.5	10.2
	6	3.02×10^{-3}	0.29	48.7	48.4	47.5	0.9	22.8
	7	3.00×10^{-4}	0.35	26.2	21.9	25.6	− 3.7	9.6
	8	3.00×10^{-5}	0.40	14.0	11.1	13.7	− 2.6	7.5
	9	3.02×10^{-4}	0.45	27.3	31.1	26.9	4.3	3.8
	10	3.02×10^{-3}	0.49	51.2	53.1	50.5	2.6	11.3
	1	3.03×10^{-4}	0.04	21.0	23.6			
	2	3.00×10^{-5}	0.10	11.1	8.3	10.0	− 1.7	5.2
	3	1.01×10^{-4}	0.15	16.8	17.8	15.8	2.0	10.0
	4	3.03×10^{-4}	0.20	24.0	24.8	23.0	1.8	10.8
	5	1.01×10^{-3}	0.24	35.1	35.7	34.0	1.7	9.9
	6	3.03×10^{-3}	0.29	48.9	48.7	47.6	1.1	17.9
	7	3.00×10^{-4}	0.35	26.3	22.0	25.7	− 3.7	9.5
	8	3.01×10^{-5}	0.40	13.9	11.0	13.7	− 2.7	7.4
	9	3.03×10^{-4}	0.45	27.4	31.2	26.9	4.3	4.0
	10	3.03×10^{-3}	0.50	51.3	53.2	50.5	2.7	13.8
1750	1	3.02×10^{-4}	0.04	13.6	15.5			
	2	3.00×10^{-5}	0.10	6.8	4.8	6.1	− 1.3	4.9
	3	1.01×10^{-4}	0.14	10.6	11.3	10.0	1.3	9.9
	4	3.02×10^{-4}	0.19	15.7	16.6	15.1	1.5	7.4
	5	1.01×10^{-3}	0.24	23.9	24.4	23.1	1.3	8.0
	6	3.02×10^{-3}	0.29	34.3	34.2	33.4	0.8	12.4
	7	3.01×10^{-4}	0.35	17.5	14.1	17.2	− 3.0	7.1
	8	3.01×10^{-5}	0.40	8.7	6.7	8.5	− 1.9	4.0
	9	3.02×10^{-4}	0.45	18.1	21.2	17.8	3.4	2.4
	10	3.02×10^{-3}	0.50	35.9	37.7	35.3	2.4	10.2

REFERENCES

1. R.T. Torgerson: *Space/Aeronaut.*, 1963, vol. 40(1), pp. 99–103.
2. J. Wadsworth, C.A. Roberts, and E.H. Rennhack: *J. Mater. Sci.*, 1982, vol. 17(9), pp. 2539–46.
3. J. Wadsworth, S.E. Dougherty, P.A. Kramer, and T.G. Nieh: *Scr. Metall. Mater.*, 1992, vol. 27(1), pp. 71–76.
4. O.D. Sherby and P.M. Burke: *Prog. Mater. Sci.*, 1968, vol. 13, pp. 325–90.
5. J.E. Bird, A.K. Mukherjee, and J.E. Dorn: In D.G. Brandon and A. Rosen, eds., *International Conference on Quantitative Relation Between Properties and Microstructure*, Israel Universities Press, Haifa, Israel, 1969, pp. 255–342.
6. W.R. Cannon and O.D. Sherby: *Metall. Trans. A*, 1970, vol. 1, pp. 1030–32.
7. F.A. Mohamed and T.G. Langdon: *Acta Metall.*, 1974, vol. 22(6), pp. 779–88.
8. P. Yavari, F.A. Mohamed, and T.G. Langdon: *Acta Metall.*, 1981, vol. 29(8), pp. 1495–1507.
9. J. Weertman: *J. Appl. Phys.*, 1957, vol. 28(10), pp. 1185–89.
10. J. Weertman: *Trans. Metall. Soc. AIME*, 1960, vol. 218, pp. 207–18.
11. S. Takeuchi and A. Argon: *Acta Metall.*, 1976, vol. 24(10), pp. 883–89.
12. M.J. Mills, J.C. Gibeling, and W.D. Nix: *Acta Metall.*, 1985, vol. 33(8), pp. 1503–14.
13. M.J. Mills, J.C. Gibeling, and W.D. Nix: *Acta Metall.*, 1986, vol. 34(5), pp. 915–25.
14. T.J. Bennett, IV and E.M. Taleff: *Microsc. Microanal.*, 2024. https://doi.org/10.1093/mam/ozae092.
15. ASTM International: *Standard Designation B654/B654M–10R18*, ASTM International, West Conshohocken, PA, 2018.
16. P.E. Armstrong and H.L. Brown: *ASM Trans. Q.*, 1965, vol. 58(1), pp. 30–37.
17. P.E. Armstrong, J.M. Dickinson, and H.L. Brown: *Trans. Metall. Soc. AIME*, 1966, vol. 236(10), pp. 1404–08.

18. E.A.D. Brady and E.M. Taleff: *Metall. Mater. Trans. A*, 2021, vol. 52A(3), pp. 1095–1105.
19. E.A.D. Brady: PhD thesis, The University of Texas at Austin, 2021.
20. P.J. Noell: PhD thesis, The University of Texas at Austin, 2015.
21. G.E. Dieter: *Mechanical Metallurgy*. McGraw-Hill, 1986.
22. M.A. Burke and W.D. Nix: *Acta Metall.*, 1975, vol. 23, pp. 793–98.
23. J.W. Hutchinson and H. Obrecht: *Fracture*, 1977, vol. 1, pp. 101–16.
24. ASTM International: *Standard Designation ASTM E112–13*, ASTM International, West Conshohocken, PA, 2013.
25. S.A. Saltykov: *Steremetricheskaya Metallograpfiya (Stereometric Metallurgy)*. Metallurgizdat, Moscow, 2nd ed., 1958.
26. E.A.D. Brady and E.M. Taleff: *Metall. Mater. Trans. A*, 2022, vol. 53(10), pp. 3057–72.
27. O.D. Sherby: *Acta Metall.*, 1962, vol. 10(2), pp. 135–47.
28. C.R. Barrett, A.J. Ardell, and O.D. Sherby: *Trans. Metall. Soc. AIME*, 1964, vol. 230, pp. 200–204.
29. F.F. Schmidt and H.R. Ogden: *Technical Report DMIC Report 188 (AD 426255)*, Defense Metals Information Center, Battelle Memorial Institute, Columbus, Ohio, 1963.
30. C.C. Wojcik: *MRS Online Proc. Libr.*, 1993, vol. 322, pp. 519–30.
31. T.S. Lundy, F.R. Winslow, R.E. Pawel, and C.J. McHargue: *Trans. Metall. Soc. AIME*, 1965, vol. 233(8), pp. 1533–9.
32. R.E. Einziger, J.N. Mundy, and H.A. Hoff: *Phys. Rev. B*, 1978, vol. 17(2), pp. 440–8.
33. W.F. Gale and T.C. Totemeier, eds.: *Smithells Metals Reference Book*, 8th ed. Elsevier, Butterworth-Heinemann, Burlington, MA, 2004.
34. E.M. Taleff, D.R. Lesuer, and J. Wadsworth: *Metall. Mater. Trans. A*, 1996, vol. 27A(2), pp. 343–52.
35. E.M. Taleff, G.A. Henshall, T.G. Nieh, D.R. Lesuer, and J. Wadsworth: *Metall. Mater. Trans. A*, 1998, vol. 29A(3A), pp. 1081–91.
36. G.A. Henshall, M.E. Kassner, and H.J. McQueen: *Metall. Trans. A*, 1992, vol. 23A, pp. 881–9.
37. E.M. Taleff, P.J. Nevland, and S.J. Yoon: In E.M. Taleff, C.K. Syn, and D.R. Lesuer, eds., *Deformation, Processing, and Properties of Structural Materials*, TMS, Warrendale, PA, 2000, pp. 373–84.
38. E.M. Taleff, P.J. Nevland, and P.E. Krajewski: *Metall. Mater. Trans. A*, 2001, vol. 32A(5), pp. 1119–30.
39. E.M. Taleff: *Key Eng. Mater.*, 2010, vol. 433, pp. 259–65.
40. E.M. Taleff, W.P. Green, M.-A. Kulas, T.R. McNelley, and P.E. Krajewski: *Mater. Sci. Eng., A*, 2005, vol. 36(5), pp. 1249–61.
41. J.-K. Chang, K. Takata, K. Ichitani, and E.M. Taleff: *Mater. Sci. Eng., A*, 2010, vol. 527, pp. 3822–8.
42. A.J. Carpenter, A.R. Antoniswamy, J.T. Carter, L.G. Hector, Jr., and E.M. Taleff: *Acta Mater.*, 2014, vol. 68, pp. 254–66.
43. J.M. Rosenberg and H.R. Piehler: *Metall. Trans.*, 1971, vol. 2(1), pp. 257–9.
44. R.H. Titran and W.D. Klopp: *NASA Technical Paper 1727*, NASA Lewis Research Center, Cleveland, OH, 1980.
45. S. Karashima, T. Iikubo, and H. Oikawa: *Trans. Jpn. Inst. Met.*, 1972, vol. 13(3), pp. 176–81.
46. C. Young and O. Sherby: 1973, *J. Iron and Steel Inst. London*, 211(9), pp. 640–47.
47. S. Robinson, C. Young, and O. Sherby: *J. Mater. Sci.*, 1974, vol. 9(2), pp. 341–43.
48. O.D. Sherby, R.H. Klundt, and A.K. Miller: *Metall. Trans. A*, 1977, vol. 8A(6), pp. 843–50.
49. M. Kassner and M. McMahon: *Metall. Trans. A*, 1987, vol. 18(5), pp. 835–46.
50. T.J. Bennett, IV and E.M. Taleff: *Metall. Mater. Trans. A*, 2024, vol. 55(2), pp. 429–46.
51. ASTM International: *Standard Designation ASTM B393–18*, ASTM International, West Conshohocken, PA, 2018.
52. F. Roux and A. Vignes: *Rev. Phys. Appl.*, 1970, vol. 5(3), pp. 393–405.
53. N. Zou, H.J. Lu, and X.G. Lu: *J. Alloys Compd.*, 2019, vol. 803, pp. 684–8.
54. A.H. Cottrell and M.A. Jaswon: *Proc. R. Soc. A*, 1949, vol. 199A(1056), pp. 104–14.
55. H.W. King: *J. Mater. Sci.*, 1966, vol. 1, pp. 79–90.
56. R.W. Buckman: In J.L. Walter, M.R. Jackson, and C.T. Sims, eds., *Alloying*, ASM International, 1988, pp. 419–45.
57. R.H. Titran, and R.W. Hall:*NASA Technical Note D-3222*, NASA Lewis Research Center, Cleveland, OH, 1966.
58. H.E. McCoy: *J. Less-Common Met.*, 1965, vol. 8(1), pp. 20–35.
59. H.E. McCoy: *ASM Trans. Q.*, 1966, vol. 59(2), pp. 277–87.
60. D. Hull and D.J. Bacon: *Introduction to Dislocations*. Elsevier/Butterworth-Hienemann, Burlington, MA, 5th ed., 2011.
61. M.A. Kulas, W.P. Green, E.M. Taleff, P.E. Krajewski, and T.R. McNelley: *Metall. Mater. Trans. A*, 2005, vol. 36A(5), pp. 1249–61.
62. G.I. Taylor: *Proc. R. Soc. London Ser. A*, 1934, vol. 145(855), pp. 362–87.
63. C. Zener and J.H. Hollomon: *J. Appl. Phys.*, 1944, vol. 15(1), pp. 22–32.
64. M.J. Klein and A.G. Metcalfe: *Metall. Trans.*, 1973, vol. 4(10), pp. 2441–48.
65. R.A. Perkins and E.S. Wright: *J. Test. Eval.*, 1974, vol. 2(5), pp. 337–43.
66. C. Himmelblau, M. Kibrick, J. Runkle, A. Joshi, J. Wadsworth, and J. Moncur: *Prog. Powder Metall.*, 1984, vol. 39, pp. 525–42.
67. R.L. Fullman, R.P. Carreker, and J.C. Fisher: *Trans. AIME*, 1953, vol. 197, pp. 657–59.
68. M.K. Kumawat, M.Z. Alam, A. Kumar, K. Gopinath, S. Saha, V. Singh, V. Srinivas, and D.K. Das: *Surf. Coat. Technol.*, 2018, vol. 349, pp. 695–706.
69. N.R. Philips, M. Carl, and N.J. Cunningham: *Metall. Mater. Trans. A*, 2020, vol. 51A(7), pp. 3299–3310.
70. O. Mireles, O. Rodriguez, Y. Gao, and N. Philips: in *AIAA Propulsion and Energy 2020 Forum*, AIAA, 2020, pp. 1–13.
71. P.D. Awasthi, P. Agrawal, R.S. Haridas, R.S. Mishra, M.T. Stawovy, S. Ohm, and A. Imandoust: *Mater. Sci. Eng. A*, 2022, vol. 831, pp. 142183.
72. B.J. Colón, K.I. Watanabe, T.J. Hobbs, C.J. Romnes, O.R. Mireles, L.E. Murr, and F. Medina: *J. Mater. Res. Technol.*, 2024, vol. 30, pp. 5028–39.
73. K.M. Mullin, C. Frey, J. Lamb, S.K. Wu, M.P. Echlin, and T.M. Pollock: *Mater. Des.*, 2024, vol. 238, pp. 112726.
74. N. Philips, C. Rock, N. Cunningham, J. Cooper, and T. Horn: *Metall. Mater. Trans. A*, 2024, vol. 55(7), pp. 2472–84.